

Article

The Imaging X-ray Polarimetry Explorer (IXPE) and New Directions for the Future

Paolo Soffitta 

Istituto di Astrofisica e Planetologia Spaziali (INAF-IAPS), Via Fosso del Cavaliere 100, 00133 Rome, Italy; paolo.soffitta@inaf.it

Abstract: An observatory dedicated to X-ray polarimetry has been operational since 9 December 2021. The Imaging X-ray Polarimetry Explorer (IXPE), a collaboration between NASA and ASI, features three X-ray telescopes equipped with detectors sensitive to linear polarization set to 120° . This marks the first instance of a three-telescope SMEX mission. Upon reaching orbit, an extending boom was deployed, extending the optics and detector to a focal length of 4 m. IXPE targets each celestial source through dithering observations. This method is essential for supporting on-ground calibrations by averaging the detector's response across a section of its sensitive plane. The spacecraft supplies power, enables attitude determination for subsequent on-ground attitude reconstruction, and issues control commands. After two years of observation, IXPE has detected significant linear polarization from nearly all classes of celestial sources emitting X-rays. This paper outlines the IXPE mission's achievements after two years of operation in orbit. In addition, we report developments for future high-throughput X-ray optics that will have much smaller dead-times by using a new generation of Applied Specific Integrated Circuits (ASIC), and may provide 3D reconstruction of photo-electron tracks.

Keywords: astrophysics; X-rays; polarimetry; gas detectors; X-ray optics; ASICs



Citation: Soffitta, P. The Imaging X-ray Polarimetry Explorer (IXPE) and New Directions for the Future. *Instruments* **2024**, *8*, 25. <https://doi.org/10.3390/instruments8020025>

Academic Editors: Matteo Duranti and Valerio Vagelli

Received: 4 January 2024
Revised: 12 March 2024
Accepted: 15 March 2024
Published: 25 March 2024



Copyright: © 2024 by the author. Licensee MDPI, Basel, Switzerland. This article is an open access article distributed under the terms and conditions of the Creative Commons Attribution (CC BY) license (<https://creativecommons.org/licenses/by/4.0/>).

1. Introduction

Cyclotron emission, synchrotron emission, and non-thermal bremsstrahlung [1–3] are the most common emission processes in X-ray astronomy providing polarized radiation. Even if emitted as intrinsically non-polarized thermal radiation, radiation can become polarized via scattering in accretion disks, blobs, and accreting columns, which are structures commonly found in astrophysical sources [4,5].

Moreover, X-ray polarimetry can probe isolated neutron stars such as magnetars, as well as neutron stars in binary systems, uncovering the long-sought quantum electrodynamics effect of vacuum birefringence [6–8]. Despite theorists' expectations for the reasons mentioned above, until very recently the only notable detection was the measurement of polarization from the Crab Nebula [9]. At the time this was a significant measurement, as it confirmed for the first time the extension of synchrotron emission to X-rays in this source.

In fact, a new generation of X-ray detectors [10–12], the Gas Pixel Detectors (GPDs), has allowed polarization to be measured by means of the photoelectric effect in gas. Using this device, we designed a space mission providing sensitive measurement in the classical energy band of X-ray astronomy. Although some Chinese colleagues had previously launched a CubeSat mission equipped with a single Gas Pixel Detector (GPD) and a collimator before IXPE, achieving low-significance results on bright galactic sources over months-long observing times [13–17], it has become evident that sensitive polarimetry requires a substantial number of detected photons. This level of sensitivity can be achieved through the use of X-ray mirrors.

Imaging polarimetry's advancements and the launch of the Imaging X-ray Polarimetry Explorer (IXPE) [18,19] have made X-ray polarimetry a standard tool in astrophysics, akin to

its use at other wavelengths for the first time. IXPE's data are publicly accessible, allowing every scientist to utilize this newly available resource.

While in the future we aim to conduct experiments with optics having a large throughput, the present ASIC of IXPE suffers from high dead time. While a five-fold improved ASIC has already been obtained by INFN, for very large optics a much larger step forward remains necessary. Below, we describe how a new generation of digital ASICs with a parallel readout allows for a drastic reduction in dead time, accompanied by the possibility of 3D imaging of the photoelectron track. Such ASICs promise to devise a photoelectric X-ray polarimeter with a dead time compliant with future high-throughput X-ray missions.

2. The IXPE Mission in Summary

IXPE, as the 14th Small Explorer (SMEX) NASA mission in partnership with ASI, was built under the supervision of NASA-MSFC (the PI institution; Philip E. Kaaret serves as PI, with Martin Weisskopf as emeritus). INAF, INFN, and industrial partner OHB-Italia devised, built, tested, and calibrated the three Detector Units, plus one spare unit, containing the GPD, the filter and onboard calibration system and the payload computer named the Detector Service Unit (DSU).

The IXPE mission, along with its optics and instrumentation [18–20], is shown operating in orbit in Figure 1.

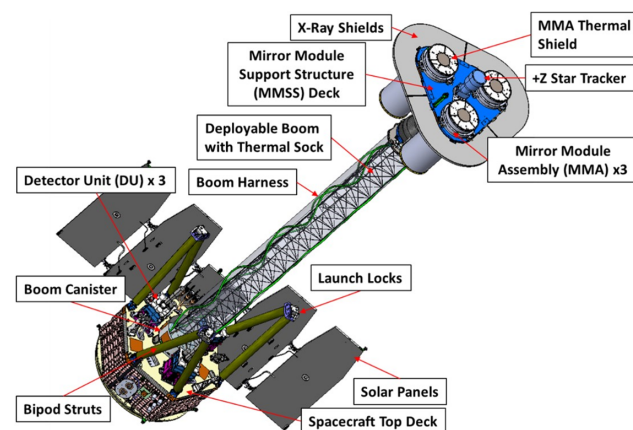


Figure 1. Elements of the deployed IXPE mission [18].

NASA-MSFC fabricated and calibrated three mirror modules [20] with the contribution of Nagoya University (thermal shields) along with one spare unit. An instrument located in the service module at the mirror focal plane, provided by ASI and composed of three detector units [19,21], is separated from the mirror by a focal length of 4 m.

The IXPE spacecraft has a global positioning system (GPS), allowing for the timing of the events with μs accuracy. Two other star trackers (rear and front) are employed to correct images after dithering by using photon-by-photon ground transmission. An X-ray shield, in conjunction with stray-light collimators on top of each Detector Unit (hereafter DU), absorbs cosmic background X-ray photons originating from outside the field of view. An ion–UV filter is located on top of each DU [22].

The DU calibration system [23] is composed of commercial ^{55}Fe isotopes (see Figure 2) with a K_{α} line at 5.89 keV and a K_{β} line at 6.5 keV. Polarized radiation at 3 keV (by means of a silver target) and 5.9 keV is produced through 45° Bragg reflection off a graphite mosaic crystal (Cal-A). Unpolarized 5.9 keV and 6.5 keV X-rays (spot ~ 3 mm and flood $\sim 15 \times 15$ mm) are source Cal-B and source Cal-C, respectively. Finally, source Cal-D uses a silicon target that produces a wide beam at 1.7 keV ($\text{Si } K_{\alpha}$) thanks to a ^{55}Fe . Cal sources are used during flight operations and Earth occultation. Cal-C and Cal-D provide the final gain correction for energy determination.

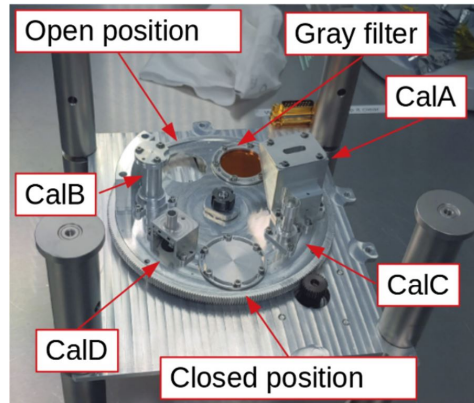


Figure 2. The filter and calibration wheel (FCW) inside each detector unit for onboard calibration. In addition to the calibration system, the FCW hosts a filter made of kapton for high-flux sources and an aluminum cap used for gathering the background.

A residual [24] miscalibration of a few (2–3) tens of eV is irreducible; this is possibly caused by the gas gain decrement due to ions and secondary electrons attaching to the exposed dielectric surface of the Gas Electron Multiplier (GEM) (charging). Because this effect is rate- and energy-dependent, it may differ during flight calibration and during observation of celestial sources [24]. An extensible boom covered with a thermal sock and thermal shields for the mirrors completes the payload system.

The IXPE mirrors (see Figure 3a) were fabricated using the classical technique of replica of electro-formed nickel–cobalt shells. The main design of the IXPE mission was based on Pegasus-XL fairing; thus, the very small thickness of the mirror shell allows for both light weight and the necessary effective area (see Figure 3b). Eventually, the Falcon-9 launcher was adopted after a competitive tender. The Falcon 9 rocket is shown in Figure 4.



Figure 3. (a) Top view of a mirror fabricated by NASA-MSFC and (b) effective area of each flight mirror [20].



Figure 4. The Falcon-9 rocket and its firing before being attached at the launch pad.

The IXPE DUs performed as expected after on-ground calibration using both polarized and unpolarized monochromatic X-ray sources (see [24]). After extensive ground calibration at INAF-IAPS [25], the three flight DUs were electrically integrated into the flight Detector Service Unit at the same laboratories (see Figure 5) on the optical bench. The instrumentation underwent extensive laboratory testing, including all of the available payload operation modes.

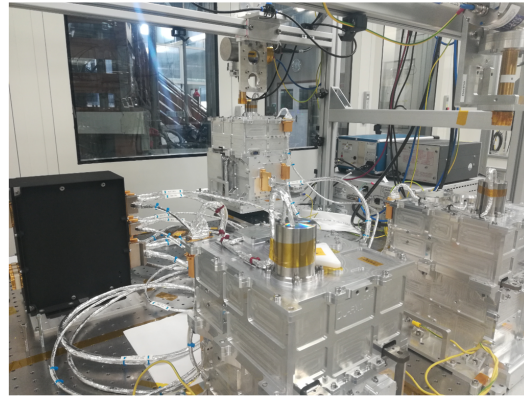


Figure 5. The three detector units integrated into the Detector Service Unit on the optical bench.

The initial analysis of IXPE data revealed that the source counting rate measured by Detector Unit 1 was somewhat higher compared to those measured by Detector Units 2 and 3. The initial response matrices did not accurately account for the differing pressures of the gas mixture inside the detectors. Consequently, this led to a variance in the detected photon flux at a given energy (notably at 1 keV, referred to as the normalization) when observing celestial sources with DU2 and DU3. This issue has since been addressed with updated response matrices that more accurately reflect the time-dependent absorption of dimethyl ether by components within the Gas Pixel Detector (GPD).

Indeed, the efficiency of the three detectors slightly diminishes with time because of the absorption of dimethyl ether by the epoxy used for sealing the detector body (Supreme 10HT by Masterbond) and possibly by the beryllium window support structure. The internal gas pressure is asymptotic, with a slow time constant of 2–3 years and a fast time constant of 1 month, as shown in [24].

However, the modulation factor is slightly better due to the increased track length, meaning that the decrease in sensitivity is not dramatic. The introduction of weights (the asymmetric tracks weigh more) [26] provides 13% better sensitivity with respect to the unweighted analysis. HEASARC analysis tools allow weighted analysis to be available to the general user. In addition, a neural network weighted analysis approach [27–29] was developed, with an improvement of about 8% with respect to the standard weighted moment analysis [30].

IXPE was designed to fit in a Pegasus-XL launcher. After the launch, we discovered a boom motion due to sunlight-to-night thermal expansion (see Figure 6). We used the portion of the orbit with active star trackers (front or rear) and the temperature sensors on the payload to model the (~ 1 arcmin) shift. Eventually, this very accurate modeling was included in the flight pipeline to make it transparent to the general user.

In contrast to the first two years of operation, when the IXPE collaboration was carried out based on the observation plan, general observers with a competitive tender managed by HEASARC now decide on the new observations. The IXPE collaboration consisted of about 190 scientists, including about 90 participants from about thirteen countries worldwide.

Table 1 summarizes the sources observed during the first two years. The largest group is for binary neutron star and blazar science. The magnetars and SNR group required the largest observing time. Bright source observations are followed by dim sources due to the small size of the onboard memory and the constraints of the S band used at the ASI Ground

Station for receiving data, located at Malindi, Kenya. A gray filter is used to cope with the very high flux. We successfully used the gray filter during the observation of Sco X-1 and the target of opportunity source Swift J1727.8-1613.

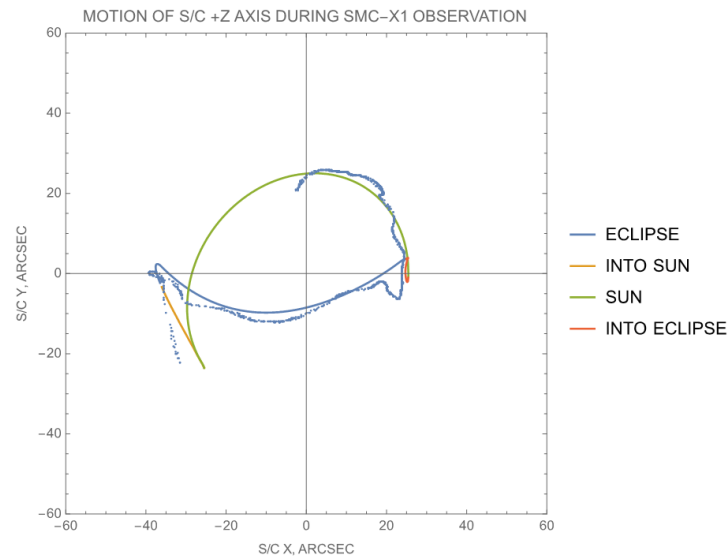


Figure 6. Boom motion due to thermal–elastic expansion along the orbit, as accurately modeled and corrected thanks to post facto reconstruction to remove the dithering [31].

Table 1. Celestial sources observed by IXPE during the first two years of operations.

WGs	Sources Observed
PWN and Pulsars	Crab Nebula and pulsar, Vela PWN, MSH 15-52, PSR B0540-69
SNR	Cas A, Tycho SNR, SN 1006 NE, RCW86, RX J1713.7-3, G21.5-0.9, Vela Jr.
BH-BN	Cyg X-1, 4U 1630-47, LMC X-1, Cyg X-3, 4U 1957 + 115, LMC X-3, Swift J1727.8-1613
NS-BN	Cen X-3, Her X-1, GS 1826-238, Vela X-1, Cyg X-2, GX301-2, X Persei, XTE J1701-462, GX9 + 9, Swift J0243.6 + 6124, IC 4329A, GRO J1008-57, EXO 2030 + 37, LS V + 44 17GX 5-1, GX 13 + 1, SMC X-1
Magnetars	4U 0142 + 61, 1RXS J170849.0, SGR 1806-20, 1E 2259 + 586
RQ-AGN	Sgr A* Complex, MCG-05-23-16, Circinus galaxy, NGC 4151, NGC1068
RL-AGN and Blazars	Mrk 501, S5 0716 + 714, 1ES 1959 + 650, Mrk 421, BL Lac, 3C 454.3, PG1553 + 113, 3C 273, 3C 279, 1ES 0229 + 20, S4 0954 + 65, 3C 454.3, PKS2155-304

Table 2 shows the celestial sources for which a significance larger than 6σ was arrived at from quick-look analysis of their polarization. This is a very limited list, as this analysis does not resolve polarimetry in terms of the angle, energy, or time, and as no background rejection [32] or subtraction was applied. Indeed, we detected significant polarization for a much larger number of sources (about 70%) by exploiting this capability once the full capabilities of IXPE were utilized.

Table 2. Quick-look analysis results providing polarimetry with a significance larger than 6σ . * Cas A, Tycho SNR, and SN 1006 show significant polarization when angularly resolved. † NGC4151 and Circinus galaxy show significant polarization when the background and energy selection are correctly taken into account.

WGs	Celestial Sources
WG1	Crab Nebula and pulsar, Vela PWN, MSH 15-52, G21.5-0.9
WG2	none *
WG3	Cyg X-1, 4U 1630-47, Cyg X-3, LMC-X3, Swift J1727.8-1613
WG4	Cen X-3, Her X-1, GX301-2, X Persei XTE J1701-462, GX9 + 9, Swift J0243.6 + 6124 GRO J1008-57, LSV 44-17, GX 5-1, Swift J0243.6 + 6124, Sco X-1, GX 13 + 1
WG5	4U 0142 + 61, 1RXS J170849.0, SGR 1806-20, 1E 2259 + 586
WG6	none †
WG7	Mrk 501, Mrk 421, 1ES 0229 + 20, 3C 454.3, 1ES 1959 + 650

The Main Limitation of IXPE

Although a significant success (see Appendix A), the achievements of IXPE in X-ray polarimetry suggest potential for further improvement. The limited effective area of the mirrors restricted the ability to conduct comprehensive ‘population studies’. In practice, only the brightest X-ray sources from each category were within reach. Future designs aim for much larger mirror areas, as envisioned for eXTP and Athena. Although Athena does not include a polarimeter, its design goal is to achieve a square meter of effective area. However, such large telescopes cannot utilize the current ASIC technology of IXPE, even considering recent advancements, as noted in [33] (see Section 3).

Additionally, IXPE’s results indicate that a promising direction for future missions would involve wide-band X-ray polarimetry extending beyond 8 keV. This approach would enhance the analysis of celestial sources where reflection (from disks, tori, winds, molecular clouds, etc.) plays a significant role in the spectrum, a facet that IXPE is barely able to examine. The employment of large multi-layer optics could enable study of the transportation of radiation in magnetized plasma at cyclotron line energies in binary pulsars or of the dynamics between power-law and hard energy tails characteristic of magnetars. Importantly, improved capacity to handle high flux could significantly reduce calibration times, which for IXPE required 40 days per detector operating continuously. This efficiency is crucial, as many missions must limit calibration time to adhere to schedules.

3. A Possible Path to the Future of X-Ray Polarimetry

One of the main drawbacks of the GPD currently flying onboard the IXPE is the large dead time [19,21], though this is mitigated by a new version of the ASIC [33]. As a matter of fact, a drastic reduction in dead time is already possible thanks to the new generation of ASICs allowing parallel readout with digital information on the pulse amplitude. These ASICs, developed by an international collaboration and are derived from the MEDIPIX family, are the TimePIX3 [34] and the most recent TimePIX4 [35]. Their design allows for data-driven operation with dead time-free operation up to 40 Mpixels $s^{-1} cm^{-2}$ for TimePIX3 and up to 3.5 Mpixels $s^{-1} mm^{-2}$ for TimePIX4. These ASICs (see Figure 7a) allow for a sparse readout as well as simultaneous per-pixel measurement of the time of arrival (with a resolution of 1.56 ns for TimePIX3 and <200 ps for TimePIX4) and time over threshold, with the latter being proportional to the charge content for each pixel. TimePIX3 features 65,536 pixels in a square pattern, with a pixel pitch of 55 μm and a noise of 60 e_{rms} . A practical implementation of TimePIX3 as the front-end for a gas detector is the GridPix [36] configuration, where the multiplication stage is obtained by applying precise photolithographic techniques to make a metallic Micromega grid above the sensitive ASIC plane at a distance of a few tens of μm (see Figure 7b, [37]).

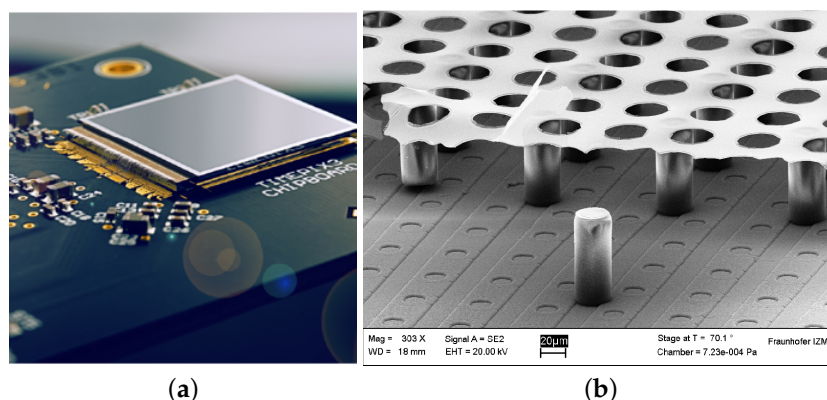


Figure 7. (a). TimePIX3 three-side buttable (<https://kt.cern/technologies/timepix3> (accessed on 17 March 2024)) and (b) Ingrid solution for the multiplication region of GridPIX [37]. The pillars are 50 μm long.

In principle, this design, allows for full 3D photoelectron track reconstruction. We previously proved the suitability of this approach for increased polarization sensitivity [38]. Before this practical implementation becomes mature enough for a space experiment, it is first necessary to: (1) prove the performance in terms of the modulation factor and lack of spurious modulation; (2) determine the energy resolution; (3) prove the resistance against heavy ion interaction with the gas; and (4) build a sealed detector body. and will be carried out in the near future.

4. Conclusions

IXPE is now a real flown polarimetry mission, and is discovering and explaining new physical phenomena in previously known X-ray sources. In addition, it is helping to disentangle geometry from physics, thereby maintaining what scientists have been promising for decades since the first rocket launches and the discoveries of OSO-8. Thanks to the perseverance of many scientists, we now are in possession of a rapidly developing observational tool to better understand a wide variety of X-ray sources and their environments. The expectations of theory can be tested with the help of accurate X-ray polarimetry. The same scientists are studying a new detector based on a modern ASIC, which promises to overcome the main limitations of the current ASIC employed onboard the IXPE.

Funding: The Imaging X-ray Polarimetry Explorer (IXPE) is a joint US and Italian mission. The US contribution is supported by the National Aeronautics and Space Administration (NASA) and led and managed by its Marshall Space Flight Center (MSFC), with industry partner Ball Aerospace (contract NNM15AA18C). The Italian contribution is supported by the Italian Space Agency (Agenzia Spaziale Italiana, ASI) through the contract ASI-OHBI-2022-13-I.0, the agreements ASI-INAF-2022-19-HH.0 and ASI-INFN-2017.13-H0, and its Space Science Data Center (SSDC) with agreements ASI-INAF-2022-14-HH.0 and ASI-INFN 2021-43-HH.0, as well as by the Istituto Nazionale di Astrofisica (INAF) and the Istituto Nazionale di Fisica Nucleare (INFN) in Italy. This research used data products provided by the IXPE Team (MSFC, SSDC, INAF, and INFN) and distributed with additional software tools by the High-Energy Astrophysics Science Archive Research Center (HEASARC) at the NASA Goddard Space Flight Center (GSFC). The author acknowledges funding from the Ministry of Universities and Research (PRIN 2020MZ884C) “Hype-X: High Yield Polarimetry Experiment in X-rays”, the INAF MiniGrant “New generation of 3D detectors for X-ray polarimetry: simulation of performances” and the MAECI Contribution 2023–2025 Grant “RES-PUBLICA Research Endeavour for Science Polarimetry with the University of Bonn in Liason with INAF for Cosmic Applications”.

Data Availability Statement: IXPE data are publicly available at <https://heasarc.gsfc.nasa.gov/docs/heasarc/missions/ixpe.html> (accessed on 17 March 2024).

Acknowledgments: The author acknowledges the IXPE Science collaboration, of which he is a part, and discussions with Klaus Desch, Jochen Kaminsky, Markus Gruber, and Vladislavs Plesanovs from the University of Bonn regarding GridPIX detectors.

Conflicts of Interest: The author declares no conflicts of interest.

Appendix A. Selected Scientific Results of IXPE

Appendix A.1. Pulsar Wind Nebulae and Radio Pulsars

Pulsar wind nebulae (PWNe) shine in X-rays emitted via the synchrotron process. Bubbles of plasma accelerated up to 10–100 TeV and magnetic fields produced by a spinning neutron star interact with the interstellar medium. These are responsible for the complex morphologies seen in X-rays. The Crab Nebula was the only source for which OSO-8 detected polarized radiation in the 1970s [9] thanks to its collimated Bragg diffraction polarimeter, and has been more recently re-detected by Polarlight [13,14]. The angularly resolved polarimetry from IXPE observations have already been published for Vela PWN [39] (see Figure A1a), the Crab Nebula and its pulsars [40] (see Figure A1b), and MSH 15-52 and its pulsars [41] (see Figure A1c). The polarization map obtained by IXPE for these two PWNe are shown in Figure A1.

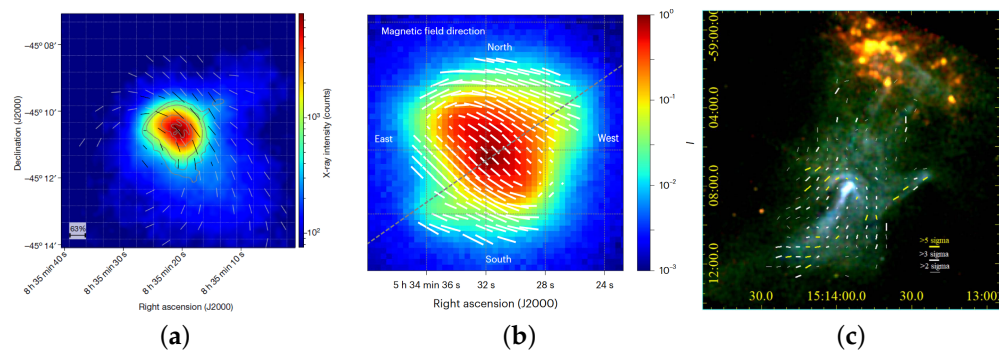


Figure A1. (a) IXPE polarization map for the Vela PWN [39]; (b) IXPE polarization map for the Crab Nebula [40]; (c) IXPE polarization map for the MSH15–52 Nebula [41].

The high level of polarization in Vela (up to 67–72%), Crab PWNe (up to 45–50%), and MSH 15-52 (up to 70%), along with the direction of the magnetic field, show that the turbulence is much less effective than expected. The IXPE image of Vela PWN shows that the polarization structure is symmetric about the projected pulsar spin axis, which corresponds to its proper direction of motion. For Crab PWN, the integrated polarization degree is 20% and the polarization angle is about 145° . While the polarization degrees are consistent between IXPE and OSO-8, the polarization angle has a small but statistically significant difference from the 154° measured [9] by OSO-8. Such a difference could be due to a change in the morphology of the inner structure of the Crab Nebula. In MSH 15-52, the magnetic field follows the thumb, fingers, and other linear structures. The polarization reaches about 70% at the end of the jet, while the magnetic field is less ordered at the base of the inner jet.

IXPE further investigated the polarization properties of the Crab and MSH 15-52 pulsars, facilitated by its imaging capabilities. For the Crab Pulsar, after subtracting the residual nebular component under the pulsar point spread function (PSF), the phase-resolved polarization properties shows significant detection only at the center of the main (P1) pulse, which is 15% with a polarization angle of about 105° . The phase-integrated polarimetry of the Crab Pulsar is $2.6^{+2.7}_{-2.6}$. Such small polarization is in contrast with most of the existing PSR models [42,43]. For MSH-1552, a single significant polarization bin at the maximum of the phase-resolved lightcurve is interpreted as a possible extension of its radio emission.

Appendix A.2. Supernova Remnants

At the time of writing, IXPE had observed five supernova remnants so far: Cas A (see Figure A2a), Tycho SNR (see Figure A2b), SN 1006 north-east rim (see Figure A2c), RCW86, and RX J1713; however, only the first three have been published [44–46]. In order to measure the polarization of Cas A [44] and Tycho SNR [45], we first selected an energy range between the calcium/argon line and the iron line, where the thermal emission is expected to be at a minimum. On the contrary, no lines are present in the SN 1006 NE limb [46], and the energy range that maximized the source-to-background ratio was selected. We then performed analysis on a pixel-by-pixel basis (see Figure A2). The results for Tycho and Cas A were inconclusive; thus, we adopted a different technique. Assuming a circular symmetry for the polarization direction, we recalculated the Stokes parameter for each event [47] by calculating a new zero for the direction of the photoelectrons and its position angle with respect to the rotated celestial coordinates, taking the center of both supernovae as the origin. This procedure resulted in new values for the Stokes parameters, providing an overall signal for the signal in all regions corresponding to the tangential and radial Q and U Stokes parameters. For every annular or circular region selected, we found that the polarization was tangential. Because synchrotron emissions require a magnetic field perpendicular to the polarization angle, we discovered that for Cas A and Tycho SNR, just as in the radio wavelength, the magnetic field has a radial global orientation. X-rays are actually emitted close to the accelerating shock fronts, and the 10–100 TeV electrons responsible for this emission have a short lifetime due to cooling. Further, interstellar magnetic fields in the outer shock (and in the reverse shock in Cas A) are eventually compressed tangentially, meaning that the instability mechanism should act quickly to realign the magnetic field in the radial direction. The tangential polarization degree for the whole Cas A emission is $1.8\% \pm 0.3\%$, which is smaller than in the radio band. The corresponding average polarization degrees for the sole synchrotron emission, considering the external shock rim, are 2.5% and 5%. For Tycho SNR, the global tangential polarization degree is $3.5\% \pm 0.7\%$, corresponding to $9.1\% \pm 2.0\%$ for the synchrotron component, while for the external rim it is $11.9\% \pm 2.2\%$. For Tycho, the levels of polarization are larger than those in the radio band. It is worth noting [45] that in Tycho SNR the west non-circular region containing the stripes shows a significant expected polarization ($\sim 23\%$), possibly indicating the presence of nonlinear diffusive shock acceleration [48].

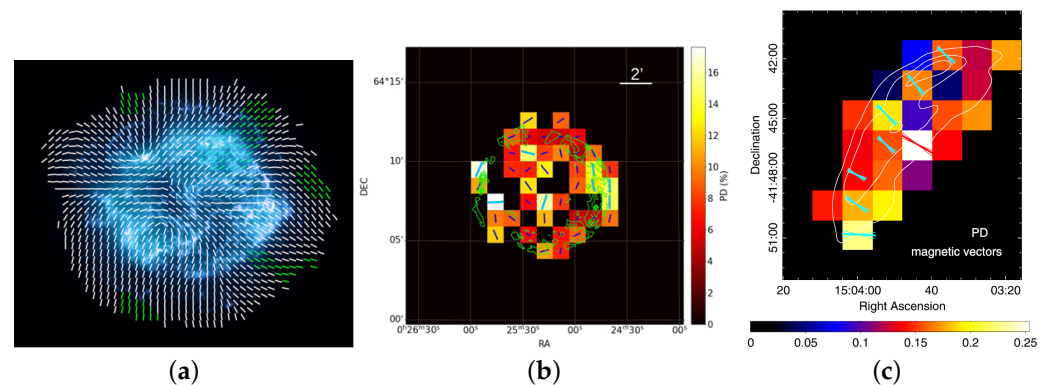


Figure A2. (a) Magnetic–field map for the Cas A SNR (Image credit: NASA/CXC/SAO/NASA/MSFC/Vink et al.). The region in green has a higher-confidence measurement. The magnetic field is mostly radial. (b) IXPE polarization map for Tycho SNR [45]. The polarization directions show a mostly radial magnetic field. (c) Polarization map for the SN 1006 NE limb [46]. The polarization directions show a mostly magnetic field perpendicular to the limb.

SN 1006 shows larger polarization than radio emissions, with an average value of about 20% for the whole shell. As in the other SNRs, the direction of the magnetic field is

perpendicular to the rim. As a matter of fact, all of the SNRs show a smaller polarization degree with respect to the maximum obtainable by synchrotron emission ($\approx 80\%$).

Appendix A.3. Accreting Stellar-Mass Black Holes

The first black hole binary system observed by IXPE was Cyg X-1 [49]. During this first point, Cyg X-1 was in a low and hard state, and the polarization found in the IXPE energy band, at $\sim 4\%$, was much larger than expected based only on the orbital inclination. This suggests a disk with its most internal part observed more edge-on than expected—a sort of warped disk. A hint of an increase in polarization with energy was found in the data as well (see Figure A3a). The other important result is that the polarization angle was found to be parallel to the radio jet (see Figure A3b). Because most of the emitted X-rays are due to the corona in the low and hard state, the polarization direction excludes a lamppost geometry (see Figure A3c). In such a geometry, the polarization angle should be perpendicular to the radio jet. The corona geometry must be sandwiched against the disk, while the polarization can be either parallel or perpendicular to the disk but the jet cannot be parallel to the disk. Thus, this is the first time that the inner flow toward the black hole has been observed to be perpendicular to the jet direction.

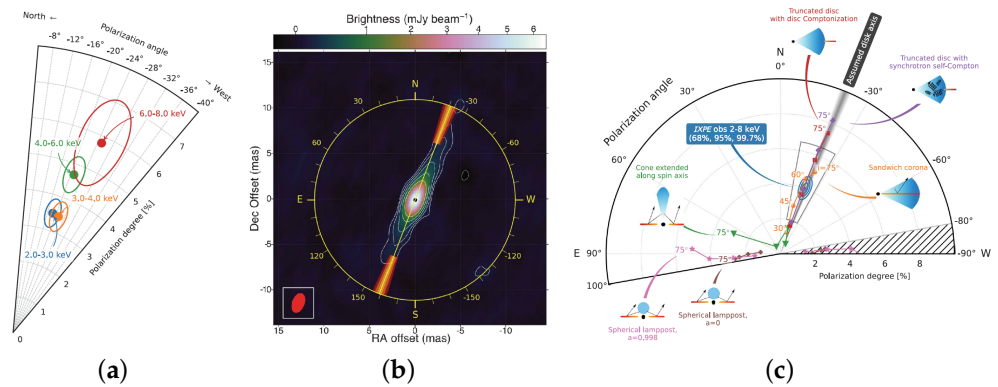


Figure A3. (a) The polarization degree shows a possible increase with energy. (b) The polarization angle is parallel to the radio jet. This discovery (1) establishes that the disk axis is parallel to the jet and (2) that the corona geometry cannot be a lamppost. (c) The different expected polarization degrees and angles for different corona models. All figures are from [49].

A sandwich corona excludes the aborted jet origin, and points to plasma instabilities across the surface. Other black holes were observed, as indicated in Table 1. The most puzzling are 4U1630-47 [50,51] and Cyg X-3 [52]. 4U1630-47 was observed at two different levels of luminosity in a high soft state where the disk emission dominates. Its complex behavior challenges a simple geometrically thin and optically thick disk model. Cyg X-3 shows polarization perpendicular to the radio ejection, thought to be due to reflection from the circumnuclear material and a polarization degree as high as $\sim 25\%$.

Appendix A.4. Accreting White Dwarfs and Neutron Stars

During the first two years of IXPE operation, we observed both low-magnetized neutron star binaries (LMNSB) and X-ray binary pulsars, with the latter being more polarized than the former. This was not unexpected, as the magnetic field is much larger for pulsars (few 10^{12} Gauss) and the photon opacity is anisotropic with respect to the magnetic field direction. In LMXRB, instead, residual polarization may derive from the scattering of primary radiation either on the accretion disk that extends down to the neutron star’s surface, from the spreading layer (the layer of material accreting onto the neutron star’s surface, which is approximately perpendicular to the accretion disk), or from the boundary layer, which is the parallel layer between the truncated disk and the neutron star surface. The sources observed thus far are listed in Table 1. Among these, Cyg X-2 [53], XTE J1702-

462 [54], GX5-1 [55], and Sco X-1 [56] are called “Z sources” because of the characteristic “Z” shape in the color–color diagram. For “Atoll”, the observed sources were GS 1826-238 [57], GX 9 + 9 [58], and 4U1830-303 [59].

X-ray pulsars show a much smaller polarization degree ($\sim 10\text{--}15\%$) than was expected ($\sim 60\text{--}80\%$) [5,60,61]. The reason for this may be that the reprocessing geometry [62] is much more complex than the simple “fan” or “pencil” model, which involves only simple columns and hot spots at the poles.

The low polarization degree found in the archetypal wind-accreting high-mass X-ray binary system Vela X-1 [63] as in the other X-Ray pulsars, could be related to the inverse temperature structure of the neutron star atmosphere, the same as for the other XRPCs. The low polarization degree found in Vela X-1 may also be due to the evolution of the polarization degree with the energy (a 90° rotation in the IXPE band) and pulse phase.

Despite the smaller than expected observed polarization, thanks to IXPE it was possible to disentangle the physics from the geometry by applying the rotating vector model derived from radio-polarimetry. For the first time, we measured the magnetic obliquity (the angle between the magnetic dipole axis and spin axis and the projection of the spin axis to the plane of the sky). Interestingly, an orthogonal rotator with magnetic obliquity close to $\sim 90^\circ$ was found by IXPE [64].

Appendix A.5. Magnetars

Magnetars are isolated neutron stars powered by an extreme magnetic field far larger than what is available on Earth, ranging from 10^{14} to 10^{15} Gauss. These very useful phenomena allow for studying photon propagation in highly magnetized atmospheres and magnetospheres. IXPE has published results from four magnetars (see Table 1), exploring their energy and phase-resolved polarization and finding very different behavior between 4U0142 + 61 [65] (see Figure A4a) and 1RXS J170849.0 [66] (see Figure A4b) in terms of their energy-resolved polarization (see Figure A4).

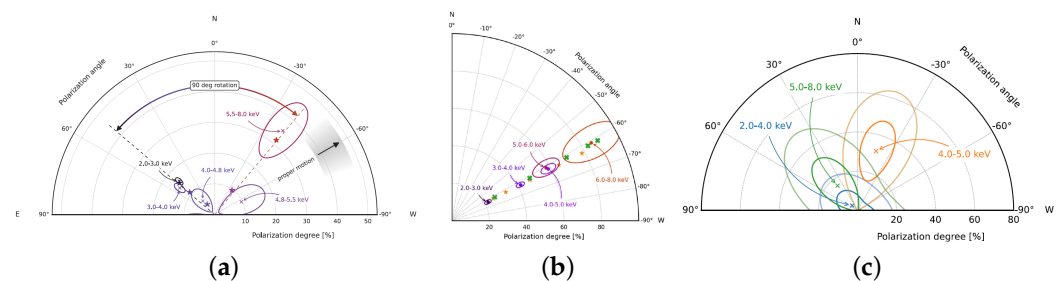


Figure A4. (a) Spectro–polarimetry for 4U0142 + 61. Crosses indicate the measured values and stars indicate the model (the equatorial belt–condensed surface RCS models are indicated by the stars). Contours enclose the 68.3% confidence level. The gray shaded area and the black arrow indicate the direction of the proper motion and its uncertainty [65]. (b) Spectro–polarimetry of 1RXS J1708, showing the 50% confidence regions for joint measurement of the polarization degree and angle. Green crosses and orange stars show the prediction of the two different possible emission regions’ structures [66]. (c) Spectro–polarimetry of SGR1806. The crosses indicate the measures. The model is frozen from the one determined by XMM (black body plus power law). The contours are 68.3% and 99% [67].

This difference is explained by the different kinds of emitting regions on the surface (i.e., geometry and physical status). Although vacuum birefringence is considered in the modeling while evaluating polarimetry expectations, the size of the emitting region is not yet sufficiently extended to require unambiguously this QED effect. A large extended region, as determined by a small pulsed fraction and a high polarization degree, are necessary for securing the vacuum birefringence at work in these systems. A third magnetar, SGR 1806-20 (see Figure A4c), was observed to be similar to 4U0142 + 61, albeit with a much smaller

significance [67], and was modeled with two hot spots placed near the magnetic equator of the bare neutron star's surface. The fourth and last magnetar observed by IXPE was 1E 2259 + 5586 [68]. For this source, as for SGR 1806, the IXPE results were interpreted in light of the spectral analysis derived from simultaneous observations with XMM. The presence of a condensed surface and a plasma loop that scatters the radiation in the magnetosphere is considered the conclusive model for this source.

In fact, the four magnetars do not show the unambiguous presence of vacuum polarization and birefringence; thus, we need to wait for observations of additional sources with a much wider emitting surface region and high polarization in order to definitively unveil them.

Appendix A.6. Radio-Quiet AGNs and Sgr A*

Accretion disks in AGNs emit mostly in the UV–optical energy band, and the primary X-ray emission is thought to be due to inverse Compton radiation in a hot corona embedding the colder accretion disk [69]. Such a geometry can produce polarized radiation [70], and from the degree of polarization it is possible to derive information on the geometry of the corona. An aborted jet origin is derived from a lamppost corona while the presence of instabilities is derived from a corona sandwiching of the accretion disk. An angle of polarization parallel to the disk axis, detected as the direction of the commonly present weakly emitting extended radio emission, is the signature of a corona sandwiching the disk. This is the case for NGC4151; indeed, the measured polarization ($4.9 \pm 1.1\%$) is thought to be entirely due to the reflection from the accretion disk. Only the upper limits [71] were found for NGC-5-23-16. Interestingly, for IXPE observation of the Circinus galaxy, a Compton-thick AGN which is observed almost edge-on with respect to its symmetry axis, confirms the presence of a thick obscuring torus as a neutral reflector due to polarization [58] ($28 \pm 7\%$). In fact, for this AGN the polarization direction is normal with respect to the weak radio jet (see Figure A5).

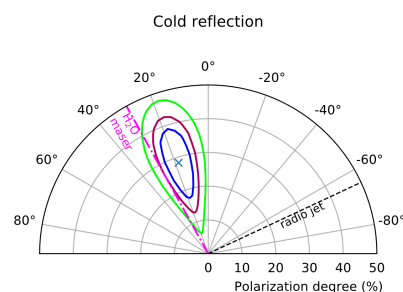


Figure A5. The polarization angle of the Circinus Galaxy is directed along the accretion disk traced by the H_2O maser shown in the figure; Together with the presence of reflection spectrum from cold matter, this is the signature of an obscuring torus responsible for the observed polarization. The polarization degree and angles contours represent 68%, 90% and 99% confidence level. Based on a comparison of the simulation and the observed polarization, the aperture of the torus is $45\text{--}55^\circ$ [58].

Much closer to us, our galactic supermassive black hole is a very dim X-ray source with occasional fast flares. Cold molecular clouds shining in X-rays may reflect [72] photons emitted in the past from Sgr A*. Thus, the reflected and observed radiation should be polarized [73], with the polarization vector indicating the origin of the radiation and, eventually, the Sgr A*. IXPE has established this for certain (see Figure A6) [74].

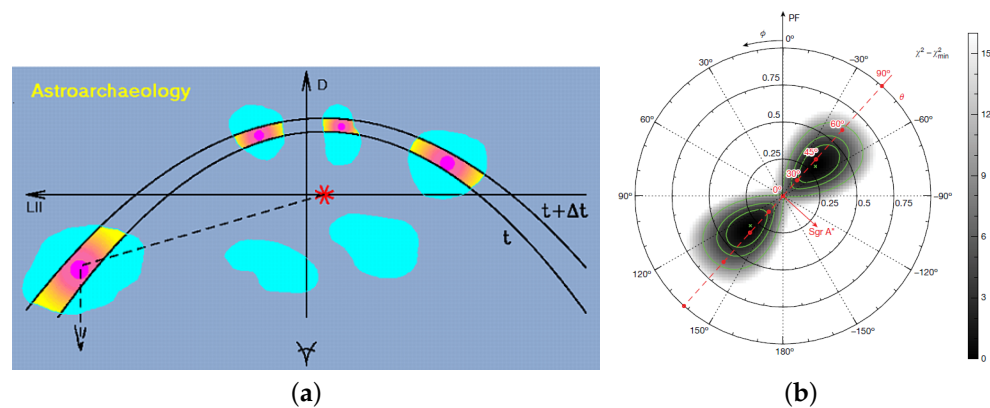


Figure A6. (a) Polarimetry map of the molecular clouds in the vicinity of the galactic center. This mapping allows the past X-ray flares of the galactic center to be reconstructed based on their polarization degree and angle. (b) Measurements taken by IXPE show that Sgr A* was 10^6 times brighter in the X-ray wavelength some 200 years ago. The mapping of different molecular clouds could allow for the determination of whether a single flare or a multiple flares occurred in the past [74].

Appendix A.7. Blazars and Radio Galaxies

The IXPE energy band is particularly suitable for analyzing blazars' polarimetry. Blazars with X-rays either in the synchrotron peak (high-synchrotron peaked HSP) or the Inverse Compton (IC) peak (low-synchrotron peaked LSP) can be probed using polarimetry. Based on the sensitivity of IXPE, only HSP blazars were found to be polarized [75–77], while LSP blazars such as BL-Lac were found to be unpolarized [78]. The upper limits remain too high to discriminate hadronic versus leptonic models as the origin of the hLIC peak [79], which was not totally unexpected given their lower fluxes. Interestingly, an observation of BL Lac (LSP) during a flare showed significant polarization, with X-rays moved into the synchrotron peak [80].

Restricting ourselves to HSP blazars such as Mrk 501 and Mrk 421, we note that for Mrk 501 IXPE observation [75] showed a polarization degree of $\sim 10\%$, which is twice as much as in the optical band, with the polarization angle directed along the jet. Together with a modest, if not null, polarization variability, these characteristic features are considered the signature of an energy-stratified shock acceleration process.

The first IXPE observation of Mrk 421 showed a polarization vector that was not coincident with the jet direction [76] but rather with a polarization degree of $(15 \pm 2)\%$, ~ 3 times larger than that observed in the optical-infrared-mm region. Another later observation surprisingly showed a polarization angle that was rotating quickly with time [77] (see Figure A7a). This rotation indicates the presence of a helical magnetic field (see Figure A7b) in addition to energy-stratified shock acceleration.

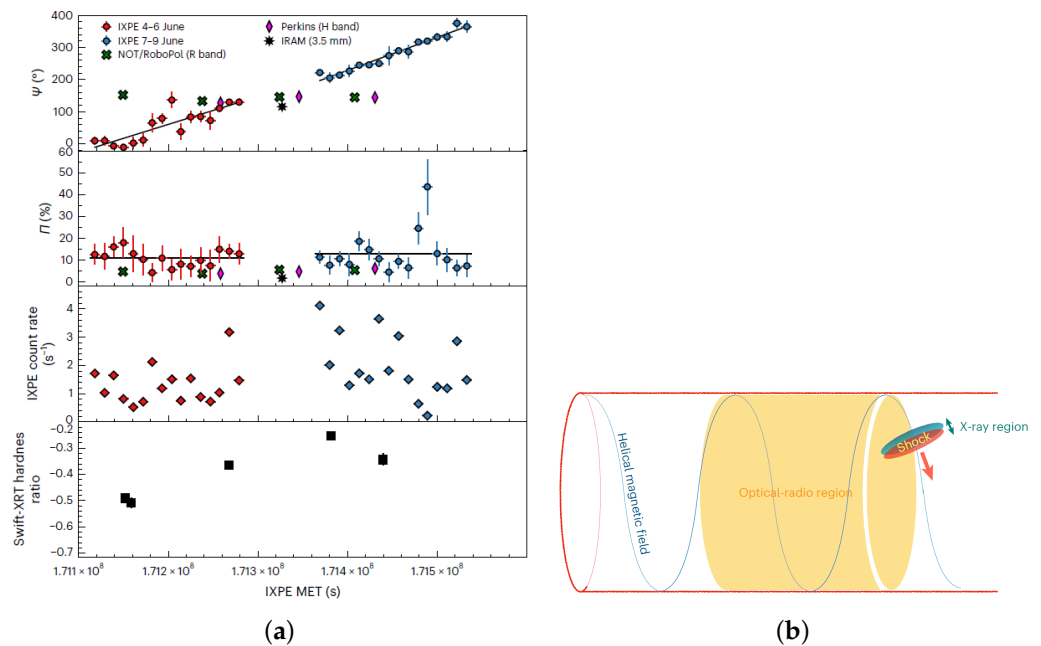


Figure A7. (a) The rotation of the polarization angle in Mrk 421 measured in X-rays is much faster (80° – 90° /day) than that previously measured in the optical band [77] (8° – 9° /day) for this source. (b) Energy-stratified shock acceleration is active in an environment embedded with a helicoidal magnetic field [77].

References

- Westfold, K.C. The Polarization of Synchrotron Radiation. *Astrophys. J.* **1959**, *130*, 241. [[CrossRef](#)]
- Gnedin, I.N.; Sunyaev, R.A. Polarization of optical and X-radiation from compact thermal sources with magnetic field. *Astron. Astrophys.* **1974**, *36*, 379–394.
- Rees, M.J. Expected polarization properties of binary X-ray sources. *Mon. Not. R. Astron. Soc.* **1975**, *171*, 457. [[CrossRef](#)]
- Sunyaev, R.A.; Titarchuk, L.G. Comptonization of low-frequency radiation in accretion disks Angular distribution and polarization of hard radiation. *Astron. Astrophys.* **1985**, *143*, 374–388. [[CrossRef](#)]
- Mészáros, P.; Novick, R.; Szentgyorgyi, A.; Chanan, G.A.; Weisskopf, M.C. Astrophysical implications and observational prospects of X-ray polarimetry. *Astrophys. J.* **1988**, *324*, 1056. [[CrossRef](#)]
- Gnedin, I.N.; Pavlov, G.G.; Shibanov, I.A. The effect of vacuum birefringence in a magnetic field on the polarization and beaming of X-ray pulsars. *Sov. Astron. Lett.* **1978**, *4*, 214.
- Ventura, J.; Nagel, W.; Meszaros, P. Possible vacuum signature in the spectra of X-ray pulsars. *Astrophys. J.* **1979**, *233*, L125. [[CrossRef](#)]
- Mészáros, P.; Ventura, J. Vacuum polarization effects on radiative opacities in a strong magnetic field. *Phys. Rev. D* **1979**, *19*, 3565. [[CrossRef](#)]
- Weisskopf, M.C.; Silver, E.H.; Kestenbaum, H.L.; Long, K.S.; Novick, R. A precision measurement of the X-ray polarization of the Crab Nebula without pulsar contamination. *Astrophys. J.* **1978**, *220*, L117. [[CrossRef](#)]
- Costa, E.; Soffitta, P.; Bellazzini, R.; Brez, A.; Lumb, N.; Spandre, G. An efficient photoelectric X-ray polarimeter for the study of black holes and neutron stars. *Nature* **2001**, *411*, 662. [[CrossRef](#)]
- Bellazzini, R.; Spandre, G.; Minuti, M.; Baldini, L.; Brez, A.; Cavalca, F.; Latronico, L.; Omodei, N.; Massai, M.M.; Sgro', C.; et al. Direct reading of charge multipliers with a self-triggering CMOS analog chip with 105 k pixels at 50 μm pitch. *Nucl. Instrum. Methods Phys. Res. A* **2006**, *566*, 552. [[CrossRef](#)]
- Bellazzini, R.; Spandre, G.; Minuti, M.; Baldini, L.; Brez, A.; Latronico, L.; Omodei, N.; Razzano, M.; Massai, M.M.; Pesce-Rollins, M.; et al. A sealed Gas Pixel Detector for X-ray astronomy. *Nucl. Instrum. Methods Phys. Res. A* **2007**, *579*, 853. [[CrossRef](#)]
- Feng, H.; Jiang, W.; Minuti, M.; Wu, Q.; Jung, A.; Yang, D.; Citraro, S.; Nasimi, H.; Yu, J.; Jin, G.; et al. PolarLight: A CubeSat X-ray polarimeter based on the gas pixel detector. *Exp. Astron.* **2019**, *47*, 225–243. [[CrossRef](#)]
- Feng, H.; Li, H.; Long, X.; Bellazzini, R.; Costa, E.; Wu, Q.; Huang, J.; Jiang, W.; Minuti, M.; Wang, W.; et al. Author Correction: Re-detection and a possible time variation of soft X-ray polarization from the Crab. *Nat. Astron.* **2020**, *4*, 808. [[CrossRef](#)]

15. Long, X.; Feng, H.; Li, H.; Zhu, J.; Wu, Q.; Huang, J.; Minuti, M.; Jiang, W.; Wang, W.; Xu, R.; et al. X-ray Polarimetry of the Crab Nebula with PolarLight: Polarization Recovery after the Glitch and a Secular Position Angle Variation. *Astrophys. J. Lett.* **2021**, *912*, L28. [[CrossRef](#)]
16. Long, X.; Feng, H.; Li, H.; Zhu, J.; Wu, Q.; Huang, J.; Minuti, M.; Jiang, W.; Yang, D.; Citraro, S.; et al. A Significant Detection of X-ray Polarization in Sco X-1 with PolarLight and Constraints on the Corona Geometry. *Astrophys. J.* **2022**, *924*, L13. [[CrossRef](#)]
17. Long, X.; Feng, H.; Li, H.; Kong, L.D.; Heyl, J.; Ji, L.; Tao, L.; Muleri, F.; Wu, Q.; Zhu, J.; et al. X-ray Polarimetry of the Accreting Pulsar 1A 0535+262 in the Supercritical State with PolarLight. *Astrophys. J.* **2023**, *950*, 76. [[CrossRef](#)]
18. Weisskopf, M.C.; Soffitta, P.; Baldini, L.; Ramsey, B.D.; O'Dell, S.L.; Romani, R.W.; Matt, G.; Deinger, W.D.; Baumgartner, W.H.; Bellazzini, R.; et al. The Imaging X-ray Polarimetry Explorer (IXPE): Pre-Launch. *J. Astron. Telesc. Instrum. Syst.* **2022**, *8*, 026002. [[CrossRef](#)]
19. Soffitta, P.; Baldini, L.; Bellazzini, R.; Costa, E.; Latronico, L.; Muleri, F.; Del Monte, E.; Fabiani, S.; Minuti, M.; Pinchera, M.; et al. The Instrument of the Imaging X-Ray Polarimetry Explorer. *Astron. J.* **2021**, *162*, 208. [[CrossRef](#)]
20. Ramsey, B.D.; Bongiorno, S.D.; Kolodziejczak, J.J.; Kilaru, K.; Alexander, C.; Baumgartner, W.H.; Breeding, S.; Elsner, R.F.; Le Roy, S.; McCracken, J.; et al. Optics for the imaging X-ray polarimetry explorer. *J. Astron. Telesc. Instrum. Syst.* **2022**, *8*, 024003. [[CrossRef](#)]
21. Baldini, L.; Barbanera, M.; Bellazzini, R.; Bonino, R.; Borotto, F.; Brez, A.; Caporale, C.; Cardelli, C.; Castellano, S.; Ceccanti, M.; et al. Design, construction, and test of the Gas Pixel Detectors for the IXPE mission. *Astropart. Phys.* **2021**, *133*, 102628. [[CrossRef](#)]
22. La Monaca, F.; Fabiani, S.; Lefevre, C.; Morbidini, A.; Piazzolla, R.; Amici, F.; Attina', P.; Brienza, D.; Costa, E.; Di Cosimo, S.; et al. IXPE DU-FM ions-UV filters characterization. In *Proceedings of the Space Telescopes and Instrumentation 2020: Ultraviolet to Gamma Ray*; den Herder, J.W.A., Nikzad, S., Nakazawa, K., Eds.; SPIE: Bellingham, WA, USA, 2021; Volume 11444, p. 1144463. [[CrossRef](#)]
23. Ferrazzoli, R.; Muleri, F.; Lefevre, C.; Morbidini, A.; Amici, F.; Brienza, D.; Costa, E.; Del Monte, E.; Di Marco, A.; Di Persio, G.; et al. In-flight calibration system of imaging x-ray polarimetry explorer. *J. Astron. Telesc. Instrum. Syst.* **2020**, *6*, 048002. [[CrossRef](#)]
24. Rankin, J.; Muleri, F.; Ferrazzoli, R.; Baldini, L.; Baumgartner, W.; Costa, E.; Del Monte, E.; Di Marco, A.; Dietz, K.; Ehlert, S.; et al. In-flight monitoring and calibration of the x-ray polarimeters on board IXPE. In *Proceedings of the UV, X-ray, and Gamma-ray Space Instrumentation for Astronomy XXIII, San Diego, CA, USA, 1–5 August 2023*; Society of Photo-Optical Instrumentation Engineers (SPIE) Conference Series; SPIE: Bellingham, WA, USA, 2023.
25. Muleri, F.; Piazzolla, R.; Di Marco, A.; Fabiani, S.; La Monaca, F.; Lefevre, C.; Morbidini, A.; Rankin, J.; Soffitta, P.; Tobia, A.; et al. The IXPE instrument calibration equipment. *Astropart. Phys.* **2022**, *136*, 102658. [[CrossRef](#)]
26. Di Marco, A.; Costa, E.; Muleri, F.; Soffitta, P.; Fabiani, S.; La Monaca, F.; Rankin, J.; Xie, F.; Bachetti, M.; Baldini, L.; et al. A Weighted Analysis to Improve the X-Ray Polarization Sensitivity of the Imaging X-ray Polarimetry Explorer. *Astron. J.* **2022**, *163*, 170. [[CrossRef](#)]
27. Peirson, A.; Romani, R.; Marshall, H.; Steiner, J.; Baldini, L. Deep ensemble analysis for Imaging X-ray Polarimetry. *Nucl. Instrum. Methods Phys. Res. Sect. A Accel. Spectrometers Detect. Assoc. Equip.* **2021**, *986*, 164740. [[CrossRef](#)]
28. Peirson, A.L.; Romani, R.W. Toward Optimal Signal Extraction for Imaging X-ray Polarimetry. *Astrophys. J.* **2021**, *920*, 40. [[CrossRef](#)]
29. Cibrario, N.; Negro, M.; Morikav, N.; Bonino, R.; Baldini, L.; Di Lalla, N.; Latronico, L.; Maldera, S.; Manfreda, A.; Omodei, N.; et al. Joint machine learning and analytic track reconstruction for X-ray polarimetry with gas pixel detectors. *Astron. Astrophys.* **2023**, *674*, A107. [[CrossRef](#)]
30. Di Marco, A.; Tennant, A.; La Monaca, F.; Muleri, F.; Rankin, J.; Rushing, J.; Soffitta, P.; Baglioni, G.; Baldini, L.; Costa, E.; et al. Validation of neural network software by using IXPE ground calibration data. In *Proceedings of the SPIE Astronomical Telescopes + Instrumentation, Montréal, QC, Canada, 31 August 2022*; den Herder, J.W.A., Nikzad, S., Nakazawa, K., Eds.; Society of Photo-Optical Instrumentation Engineers (SPIE): Bellingham, WA, USA, 2022; Volume 12181, p. 1218157. [[CrossRef](#)]
31. Soffitta, P.; Baldini, L.; Baumgartner, W.; Bellazzini, R.; Bongiorno, S.D.; Bucciantini, N.; Costa, E.; Dovčiak, M.; Ehlert, S.; Kaaret, P.E.; et al. The Imaging X-ray polarimetry explorer (IXPE) at last! In *UV, X-ray, and Gamma-ray Space Instrumentation for Astronomy XXIII*; Siegmund, O.H., Hoadley, K., Eds.; Society of Photo-Optical Instrumentation Engineers (SPIE) Conference Series; SPIE: Bellingham, WA, USA, 2023; Volume 12678, p. 1267803. [[CrossRef](#)]
32. Di Marco, A.; Soffitta, P.; Costa, E.; Ferrazzoli, R.; La Monaca, F.; Rankin, J.; Ratheesh, A.; Xie, F.; Baldini, L.; Del Monte, E.; et al. Handling the Background in IXPE Polarimetric Data. *Astron. J.* **2023**, *165*, 143. [[CrossRef](#)]
33. Minuti, M.; Baldini, L.; Bellazzini, R.; Brez, A.; Ceccanti, M.; Krummenacher, F.; Latronico, L.; Lucchesi, L.; Manfreda, A.; Orsini, L.; et al. XPOL-III: A new-generation VLSI CMOS ASIC for high-throughput X-ray polarimetry. *Nucl. Instrum. Methods Phys. Res. A* **2023**, *1046*, 167674. [[CrossRef](#)]
34. Poikela, T.; Plosila, J.; Westerlund, T.; Campbell, M.; De Gaspari, M.; Llopert, X.; Gromov, V.; Kluit, R.; van Beuzekom, M.; Zappone, F.; et al. Timepix3: A 65K channel hybrid pixel readout chip with simultaneous ToA/ToT and sparse readout. *J. Instrum.* **2014**, *9*, C05013. [[CrossRef](#)]
35. Llopert, X.; Alozy, J.; Ballabriga, R.; Campbell, M.; Casanova, R.; Gromov, V.; Heijne, E.H.M.; Poikela, T.; Santin, E.; Sriskaran, V.; et al. Timepix4, a large area pixel detector readout chip which can be tiled on 4 sides providing sub-200 ps timestamp binning. *J. Instrum.* **2022**, *17*, C01044. [[CrossRef](#)]

36. Ligtenberg, C.; Heijhoff, K.; Bilevych, Y.; Desch, K.; van der Graaf, H.; Hartjes, F.; Kaminski, J.; Kluit, P.M.; Raven, G.; Schiffer, T.; et al. Performance of a GridPix detector based on the Timepix3 chip. *Nucl. Instrum. Methods Phys. Res. A* **2018**, *908*, 18–23. [[CrossRef](#)]
37. Lupberger, M. The Pixel-TPC: First results from an 8-InGrid module. *J. Instrum.* **2014**, *9*, C01033. [[CrossRef](#)]
38. Kim, D.E.; Di Marco, A.; Soffitta, P.; Costa, E.; Fabiani, S.; Muleri, F.; Ratheesh, A.; La Monaca, F.; Rankin, J.; Del Monte, E.; et al. The future of X-ray polarimetry towards the 3-Dimensional photoelectron track reconstruction. *J. Instrum.* **2024**, *19*, C02028. [[CrossRef](#)]
39. Xie, F.; Di Marco, A.; La Monaca, F.; Liu, K.; Muleri, F.; Bucciantini, N.; Romani, R.W.; Costa, E.; Rankin, J.; Soffitta, P.; et al. Vela pulsar wind nebula X-rays are polarized to near the synchrotron limit. *Nature* **2022**, *612*, 658–660. [[CrossRef](#)] [[PubMed](#)]
40. Bucciantini, N.; Ferrazzoli, R.; Bachetti, M.; Rankin, J.; Di Lalla, N.; Sgrò, C.; Omodei, N.; Kitaguchi, T.; Mizuno, T.; Gunji, S.; et al. Simultaneous space and phase resolved X-ray polarimetry of the Crab pulsar and nebula. *Nat. Astron.* **2023**, *7*, 602–610. [[CrossRef](#)]
41. Romani, R.W.; Wong, J.; Di Lalla, N.; Omodei, N.; Xie, F.; Ng, C.Y.; Ferrazzoli, R.; Di Marco, A.; Bucciantini, N.; Pilia, M.; et al. The Polarized Cosmic Hand: IXPE Observations of PSR B1509-58/MSH 15-52. *Astrophys. J.* **2023**, *957*, 23. [[CrossRef](#)]
42. Dyks, J.; Harding, A.K.; Rudak, B. Relativistic Effects and Polarization in Three High-Energy Pulsar Models. *Astrophys. J.* **2004**, *606*, 1125–1142. [[CrossRef](#)]
43. Pétri, J. Phase-resolved polarization properties of the pulsar striped wind synchrotron emission. *Mon. Not. R. Astron. Soc.* **2013**, *434*, 2636–2644. [[CrossRef](#)]
44. Vink, J.; Prokhorov, D.; Ferrazzoli, R.; Slane, P.; Zhou, P.; Asakura, K.; Baldini, L.; Bucciantini, N.; Costa, E.; Di Marco, A.; et al. X-Ray Polarization Detection of Cassiopeia A with IXPE. *Astrophys. J.* **2022**, *938*, 40. [[CrossRef](#)]
45. Ferrazzoli, R.; Slane, P.; Prokhorov, D.; Zhou, P.; Vink, J.; Bucciantini, N.; Costa, E.; Di Lalla, N.; Di Marco, A.; Soffitta, P.; et al. X-Ray Polarimetry Reveals the Magnetic-field Topology on Sub-parsec Scales in Tycho’s Supernova Remnant. *Astrophys. J.* **2023**, *945*, 52. [[CrossRef](#)]
46. Zhou, P.; Prokhorov, D.; Ferrazzoli, R.; Yang, Y.J.; Slane, P.; Vink, J.; Silvestri, S.; Bucciantini, N.; Reynoso, E.; Moffett, D.; et al. Magnetic Structures and Turbulence in SN 1006 Revealed with Imaging X-ray Polarimetry. *Astrophys. J.* **2023**, *957*, 55. [[CrossRef](#)]
47. Kislak, F.; Clark, B.; Beilicke, M.; Krawczynski, H. Analyzing the data from X-ray polarimeters with Stokes parameters. *Astropart. Phys.* **2015**, *68*, 45–51. [[CrossRef](#)]
48. Bykov, A.M.; Ellison, D.C.; Osipov, S.M.; Pavlov, G.G.; Uvarov, Y.A. X-ray Stripes in Tycho’s Supernova Remnant: Synchrotron Footprints of a Nonlinear Cosmic-ray-driven Instability. *Astrophys. J. Lett.* **2011**, *735*, L40. [[CrossRef](#)]
49. Krawczynski, H.; Muleri, F.; Dovčiak, M.; Veledina, A.; Rodriguez Cavero, N.; Svoboda, J.; Ingram, A.; Matt, G.; Garcia, J.A.; Loktev, V.; et al. Polarized x-rays constrain the disk-jet geometry in the black hole X-ray binary Cygnus X-1. *Science* **2022**, *378*, 650–654. [[CrossRef](#)]
50. Ratheesh, A.; Dovčiak, M.; Krawczynski, H.; Podgorný, J.; Marra, L.; Veledina, A.; Suleimanov, V.; Rodriguez Cavero, N.; Steiner, J.; Svoboda, J.; et al. The high polarisation of the X-rays from the Black Hole X-ray Binary 4U 1630-47 challenges standard thin accretion disc scenario. *arXiv* **2023**, arXiv:2304.12752. [[CrossRef](#)].
51. Rodriguez Cavero, N.; Marra, L.; Krawczynski, H.; Dovčiak, M.; Bianchi, S.; Steiner, J.F.; Svoboda, J.; Capitanio, F.; Matt, G.; Negro, M.; et al. The First X-ray Polarization Observation of the Black Hole X-ray Binary 4U 1630-47 in the Steep Power Law State. *arXiv* **2023**, arXiv:2305.10630. [[CrossRef](#)].
52. Veledina, A.; Muleri, F.; Poutanen, J.; Podgorný, J.; Dovčiak, M.; Capitanio, F.; Churazov, E.; De Rosa, A.; Di Marco, A.; Forsblom, S.; et al. Astronomical puzzle Cyg X-3 is a hidden Galactic ultraluminous X-ray source. *arXiv* **2023**, arXiv:2303.01174. [[CrossRef](#)].
53. Farinelli, R.; Fabiani, S.; Poutanen, J.; Ursini, F.; Ferrigno, C.; Bianchi, S.; Cocchi, M.; Capitanio, F.; De Rosa, A.; Gnarini, A.; et al. Accretion geometry of the neutron star low mass X-ray binary Cyg X-2 from X-ray polarization measurements. *Mon. Not. R. Astron. Soc.* **2023**, *519*, 3681–3690. [[CrossRef](#)]
54. Cocchi, M.; Gnarini, A.; Fabiani, S.; Ursini, F.; Poutanen, J.; Capitanio, F.; Bobrikova, A.; Farinelli, R.; Paizis, A.; Sidoli, L.; et al. Discovery of strongly variable X-ray polarization in the neutron star low-mass X-ray binary transient XTE J1701–462. *Astron. Astrophys.* **2023**, *674*, L10. [[CrossRef](#)]
55. Fabiani, S.; Capitanio, F.; Iaria, R.; Poutanen, J.; Gnarini, A.; Ursini, F.; Farinelli, R.; Bobrikova, A.; Steiner, J.F.; Svoboda, J.; et al. Discovery of a variable energy-dependent X-ray polarization in the accreting neutron star GX 5-1. *arXiv* **2023**, arXiv:2310.06788. [[CrossRef](#)].
56. La Monaca, F.; Di Marco, A.; Poutanen, J.; Bachetti, M.; Motta, S.E.; Papitto, A.; Pilia, M.; Xie, F.; Bianchi, S.; Bobrikova, A.; et al. Highly Significant Detection of X-Ray Polarization from the Brightest Accreting Neutron Star Sco X-1. *arXiv* **2023**, arXiv:2311.06359. [[CrossRef](#)].
57. Capitanio, F.; Fabiani, S.; Gnarini, A.; Ursini, F.; Ferrigno, C.; Matt, G.; Poutanen, J.; Cocchi, M.; Mikusincova, R.; Farinelli, R.; et al. Polarization Properties of the Weakly Magnetized Neutron Star X-ray Binary GS 1826-238 in the High Soft State. *Astrophys. J.* **2023**, *943*, 129. [[CrossRef](#)]
58. Ursini, F.; Marinucci, A.; Matt, G.; Bianchi, S.; Marin, F.; Marshall, H.L.; Middei, R.; Poutanen, J.; Rogantini, D.; De Rosa, A.; et al. Mapping the circumnuclear regions of the Circinus galaxy with the Imaging X-ray Polarimetry Explorer. *Mon. Not. R. Astron. Soc.* **2023**, *519*, 50–58. [[CrossRef](#)]

59. Di Marco, A.; La Monaca, F.; Poutanen, J.; Russell, T.D.; Anitra, A.; Farinelli, R.; Mastroserio, G.; Muleri, F.; Xie, F.; Bachetti, M.; et al. First Detection of X-Ray Polarization from the Accreting Neutron Star 4U 1820-303. *Astrophys. J. Lett.* **2023**, *953*, L22. [[CrossRef](#)]
60. Caiazzo, I.; Heyl, J. Polarization of accreting X-ray pulsars. I. A new model. *Mon. Not. R. Astron. Soc.* **2021**, *501*, 109–128. [[CrossRef](#)]
61. Caiazzo, I.; Heyl, J. Polarization of accreting X-ray pulsars—II. Hercules X-1. *Mon. Not. R. Astron. Soc.* **2021**, *501*, 129–136. [[CrossRef](#)]
62. Tsygankov, S.S.; Doroshenko, V.; Poutanen, J.; Heyl, J.; Mushtukov, A.A.; Caiazzo, I.; Di Marco, A.; Forsblom, S.V.; González-Caniulef, D.; Klawin, M.; et al. The X-Ray Polarimetry View of the Accreting Pulsar Cen X-3. *Astrophys. J. Lett.* **2022**, *941*, L14. [[CrossRef](#)]
63. Forsblom, S.V.; Poutanen, J.; Tsygankov, S.S.; Bachetti, M.; Di Marco, A.; Doroshenko, V.; Heyl, J.; La Monaca, F.; Malacaria, C.; Marshall, H.L.; et al. IXPE Observations of the Quintessential Wind-accreting X-ray Pulsar Vela X-1. *Astrophys. J. Lett.* **2023**, *947*, L20. [[CrossRef](#)]
64. Tsygankov, S.S.; Doroshenko, V.; Mushtukov, A.A.; Poutanen, J.; Di Marco, A.; Heyl, J.; La Monaca, F.; Forsblom, S.V.; Malacaria, C.; Marshall, H.L.; et al. X-ray pulsar GRO J1008–57 as an orthogonal rotator. *Astron. Astrophys.* **2023**, *675*, A48. [[CrossRef](#)]
65. Taverna, R.; Turolla, R.; Muleri, F.; Heyl, J.; Zane, S.; Baldini, L.; González-Caniulef, D.; Bachetti, M.; Rankin, J.; Caiazzo, I.; et al. Polarized x-rays from a magnetar. *Science* **2022**, *378*, 646–650. [[CrossRef](#)] [[PubMed](#)]
66. Zane, S.; Taverna, R.; González-Caniulef, D.; Muleri, F.; Turolla, R.; Heyl, J.; Uchiyama, K.; Ng, M.; Tamagawa, T.; Caiazzo, I.; et al. A Strong X-Ray Polarization Signal from the Magnetar 1RXS J170849.0-400910. *Astrophys. J. Lett.* **2023**, *944*, L27. [[CrossRef](#)]
67. Turolla, R.; Taverna, R.; Israel, G.L.; Muleri, F.; Zane, S.; Bachetti, M.; Heyl, J.; Di Marco, A.; Gau, E.; Krawczynski, H.; et al. IXPE and XMM-Newton observations of the Soft Gamma Repeater SGR 1806-20. *arXiv* **2023**, arXiv:2308.01238. [[CrossRef](#)].
68. Heyl, J.; Taverna, R.; Turolla, R.; Israel, G.L.; Ng, M.; Kirmizibayrak, D.; González-Caniulef, D.; Caiazzo, I.; Zane, S.; Ehlert, S.R.; et al. The detection of polarized x-ray emission from the magnetar 1E 2259+586. *Mon. Not. R. Astron. Soc.* **2023**, *527*, 12219–12231. [[CrossRef](#)]
69. Haardt, F.; Maraschi, L. X-Ray Spectra from Two-Phase Accretion Disks. *Astrophys. J.* **1993**, *413*, 507. [[CrossRef](#)]
70. Haardt, F.; Matt, G. X-ray polarization in the two-phase model for AGN and X-ray binaries. *Mon. Not. R. Astron. Soc.* **1993**, *261*, 346–352. [[CrossRef](#)]
71. Marinucci, A.; Muleri, F.; Dovciak, M.; Bianchi, S.; Marin, F.; Matt, G.; Ursini, F.; Middei, R.; Marshall, H.L.; Baldini, L.; et al. Polarization constraints on the X-ray corona in Seyfert Galaxies: MCG-05-23-16. *Mon. Not. R. Astron. Soc.* **2022**, *516*, 5907–5913. [[CrossRef](#)]
72. Sunyaev, R.A.; Markevitch, M.; Pavlinsky, M. The center of the Galaxy in the recent past—A view from GRANAT. *Astrophys. J.* **1993**, *407*, 606–610. [[CrossRef](#)]
73. Churazov, E.; Sunyaev, R.; Sazonov, S. Polarization of X-ray emission from the Sgr B2 cloud. *Mon. Not. R. Astron. Soc.* **2002**, *330*, 817–820. [[CrossRef](#)]
74. Marin, F.; Churazov, E.; Khabibullin, I.; Ferrazzoli, R.; Di Gesu, L.; Barnouin, T.; Di Marco, A.; Middei, R.; Vikhlinin, A.; Costa, E.; et al. X-ray polarization evidence for a 200-year-old flare of Sgr A*. *Nature* **2023**, *619*, 41–45. [[CrossRef](#)]
75. Liodakis, I.; Marscher, A.P.; Agudo, I.; Berdyugin, A.V.; Bernardos, M.I.; Bonnoli, G.; Borman, G.A.; Casadio, C.; Casanova, V.; Cavazzuti, E.; et al. Polarized blazar X-rays imply particle acceleration in shocks. *Nature* **2022**, *611*, 677–681. [[CrossRef](#)]
76. Di Gesu, L.; Donnarumma, I.; Tavecchio, F.; Agudo, I.; Barnounin, T.; Cibrario, N.; Di Lalla, N.; Di Marco, A.; Escudero, J.; Errando, M.; et al. The X-ray Polarization View of Mrk 421 in an Average Flux State as Observed by the Imaging X-ray Polarimetry Explorer. *Astrophys. J. Lett.* **2022**, *938*, L7. [[CrossRef](#)]
77. Di Gesu, L.; Marshall, H.L.; Ehlert, S.R.; Kim, D.E.; Donnarumma, I.; Tavecchio, F.; Liodakis, I.; Kiehlmann, S.; Agudo, I.; Jorstad, S.G.; et al. Discovery of X-ray polarization angle rotation in the jet from blazar Mrk 421. *Nat. Astron.* **2023**, *7*, 1245–1258. [[CrossRef](#)]
78. Middei, R.; Liodakis, I.; Perri, M.; Puccetti, S.; Cavazzuti, E.; Di Gesu, L.; Ehlert, S.R.; Madejski, G.; Marscher, A.P.; Marshall, H.L.; et al. X-ray Polarization Observations of BL Lacertae. *Astrophys. J. Lett.* **2023**, *942*, L10. [[CrossRef](#)]
79. Zhang, H.; Böttcher, M. X-Ray and Gamma-Ray Polarization in Leptonic and Hadronic Jet Models of Blazars. *Astrophys. J.* **2013**, *774*, 18. [[CrossRef](#)]
80. Peirson, A.L.; Negro, M.; Liodakis, I.; Middei, R.; Kim, D.E.; Marscher, A.P.; Marshall, H.L.; Pacciani, L.; Romani, R.W.; Wu, K.; et al. X-ray Polarization of BL Lacertae in Outburst. *Astrophys. J. Lett.* **2023**, *948*, L25. [[CrossRef](#)]

Disclaimer/Publisher’s Note: The statements, opinions and data contained in all publications are solely those of the individual author(s) and contributor(s) and not of MDPI and/or the editor(s). MDPI and/or the editor(s) disclaim responsibility for any injury to people or property resulting from any ideas, methods, instructions or products referred to in the content.